binds to 30 different human PDZ domains, whereas the expressed human NS1 protein binds at a very low level or not at all (Fig. 3B). The identities of these 30 PDZ domain–containing proteins are shown in table S3 and include members of all classes of PDZ domain proteins with roles in cell polarity, T cell proliferation, and mitochondrial localization, among others.

Thus, although the molecular consequences of these interactions are as yet unknown, it appears that avian NS1 proteins, when introduced into human cells, have the opportunity to bind to and presumably disrupt many PDZ domain protein–mediated pathways that the human NS1 protein cannot. The 1957 H2N2 and the 1968 H3N2 influenza pandemics were caused by viruses in which only the surface glycoproteins HA and NA and the polymerase protein PB1 of the prevalent human strains were replaced by avian-like molecules, while the remaining core genes remained of human virus origin. In contrast, the recent H5, H7, and H9 outbreaks in Asia were caused by viruses in which the entire complement of influenza genes, including those encoding NS, were derived from an avian source. We propose that the introduction of avian NS1 into human cells can potentially disrupt many cell pathways via binding to PDZ domain–containing proteins, whereas the human NS1 does not. Disruption of these pathways at the cellular level may well contribute to the higher mortality rates reported in the recent outbreaks as compared to those seen in previous pandemics, though it is clear that multiple genes and gene products are involved. This finding reveals an entirely new means by which AIV may interact with host cell proteins, and these proteins may prove valuable as targets for antiviral therapy.

The wealth of AIV genome data provided by this sequencing project has revealed virus families showing conserved combinations of core proteins; frequent reassortment among the surface proteins; newly observed clades of the PB1, PB2, PA, and NP genes; and a possible virulence marker in NS1. We expect that further analysis of this data by the research community will be valuable in understanding AIVs and how they contribute to human disease.

References and Notes

1. T. Horimoto, Y. Kawaoka, *Nat. Rev. Microbiol.* **3**, 591 (2005).
2. The World Health Organization maintains an updated Web site of the human H5N1 cases and deaths at www.who.int/csr/disease/avian_influenza/country. The figures given here are from the 5 January 2006 update.
3. J. Liu *et al.*, *Science* **309**, 1206 (2005).
4. H. Chen *et al.*, *Nature* **436**, 191 (2005).
5. M. Enserink, *Science* **310**, 209 (2005).
6. Information on materials and methods is available as supporting material on *Science* Online.
7. P. Richterich, *Genome Res.* **8**, 251 (1998).
8. Z. Yang, *Comput. Appl. Biosci.* **13**, 555 (1997).
9. W. Chen *et al.*, *Nat. Med.* **7**, 1306 (2001).
10. Y. Kawaoka *et al.*, *Virus Res.* **55**, 143 (1998).
11. B. W. J. Mahy, in *Genetics of Influenza Viruses*, D. W. Kingsbury, P. Palese, Eds. (Springer-Verlag, Berlin, 1983), pp. 192–254.
12. R. M. Krug *et al.*, *Virology* **309**, 181 (2003).
13. S. Schultz-Cherry *et al.*, *J. Virol.* **75**, 7875 (2001).
14. A. Garcia-Sastre *et al.*, *Virology* **252**, 324 (1998).
15. S. H. Seo, R. G. Webster, *Virus Res.* **103**, 107 (2004).
16. G. K. Geiss *et al.*, *Proc. Natl. Acad. Sci. U.S.A.* **99**, 10736 (2002).
17. A. S. Lipatov *et al.*, *J. Gen. Virol.* **86**, 1121 (2005).
18. Z. Songyang *et al.*, *Science* **275**, 73 (1997).
19. M. Sheng, C. Sala, *Annu. Rev. Neurosci.* **24**, 1 (2001).
20. Single-letter abbreviations for the amino acid residues are as follows: A, Ala; C, Cys; D, Asp; E, Glu; F, Phe; G, Gly; H, His; I, Ile; K, Lys; L, Leu; M, Met; N, Asn; P, Pro; Q, Gln; R, Arg; S, Ser; T, Thr; V, Val; W, Trp; and Y, Tyr.
21. K. Wuthrich, *Nat. Struct. Biol.* **7**, 188 (2000).
22. H.-C. Wong *et al.*, *Mol. Cell* **12**, 1251 (2003).

23. We thank the following Hartwell Center staff for superb support: J. Armstrong, S. Tate, and C. Aldridge (HT Sequencing); M. Sanyang (Software Development); S. Olsen, P. Rodrigues, and B. Cassell (Macromolecular Synthesis); and S. Malone and B. Pappas (Operations). Sequences from this study have been deposited in GenBank under accession numbers CY003847 to CY006042. This work was supported by the American Lebanese Syrian Associated Charities, a Cancer Center Support Grant (CA 21765), the U.S. Public Health Service (grant AI95357), and the Hartwell Foundation.

Supporting Online Material

www.sciencemag.org/cgi/content/full/1121586/DC1
Materials and Methods
SOM Text
Figs. S1 to S15
Tables S1 to S6
References

20 October 2005; accepted 17 January 2006
Published online 26 January 2006;
10.1126/science.1121586
Include this information when citing this paper.

REPORTS

Fuel-Powered Artificial Muscles

Von Howard Ebron,[1] Zhiwei Yang,[1] Daniel J. Seyer,[1] Mikhail E. Kozlov,[1] Jiyoung Oh,[1,2] Hui Xie,[1] Joselito Razal,[1] Lee J. Hall,[1] John P. Ferraris,[1] Alan G. MacDiarmid,[1] Ray H. Baughman[1]*

Artificial muscles and electric motors found in autonomous robots and prosthetic limbs are typically battery-powered, which severely restricts the duration of their performance and can necessitate long inactivity during battery recharge. To help solve these problems, we demonstrated two types of artificial muscles that convert the chemical energy of high–energy-density fuels to mechanical energy. The first type stores electrical charge and uses changes in stored charge for mechanical actuation. In contrast with electrically powered electrochemical muscles, only half of the actuator cycle is electrochemical. The second type of fuel-powered muscle provides a demonstrated actuator stroke and power density comparable to those of natural skeletal muscle and generated stresses that are over a hundred times higher.

Although nature's choice is to chemically power the diverse muscles of her design with a high–energy-density fuel, humankind has largely taken another route. In those systems, electrical energy is typically converted to mechanical energy by means of motors, hydraulic systems, or piezoelectric, electrostrictive, or electrochemical actuators (*1*–*9*). Because of high electrical power needs, some of the most athletically capable robots cannot freely prance around because they are wired to a stationary power source.

There are exceptions to this use of electrically powered actuators: Chemically powered artificial muscles based on polymer gels were demonstrated over 50 years ago and remain of practical interest for both chemically and electrically powered actuators (*10*–*12*). Although actuator strains can be very large, their application has been limited by low response rates, low stress generation, and the low energy densities of the chemicals used for driving actuation. The combustion of fuels in a preburner has been used to indirectly power actuation of shape-memory alloys (*13*), and muscles that act as fuel cells have been proposed (*14*, *15*) but not experimentally demonstrated. Also, nanoscale and larger actuators that are powered by oxygen gas released by the catalytic decomposition of hydrogen peroxide have been described (*16*–*20*).

We experimentally demonstrated two types of artificial muscles that are powered by high–energy-density fuels (hydrogen, methanol, or formic acid). The first type uses a catalyst-containing carbon nanotube electrode that simultaneously functions as a muscle, a fuel-cell electrode, and a supercapacitor electrode. The result is a muscle that converts chemical energy in a fuel to electrical energy and can use this electrical energy for actuation, store it, or potentially use it for other energy needs. The

[1]Department of Chemistry and NanoTech Institute, University of Texas at Dallas, Richardson, TX 75083–0688, USA. [2]Research Center of Dielectric and Advanced Matter Physics and Department of Physics, Pusan National University, Busan 609–735, Korea.

*To whom correspondence should be addressed. E-mail: ray.baughman@utdallas.edu

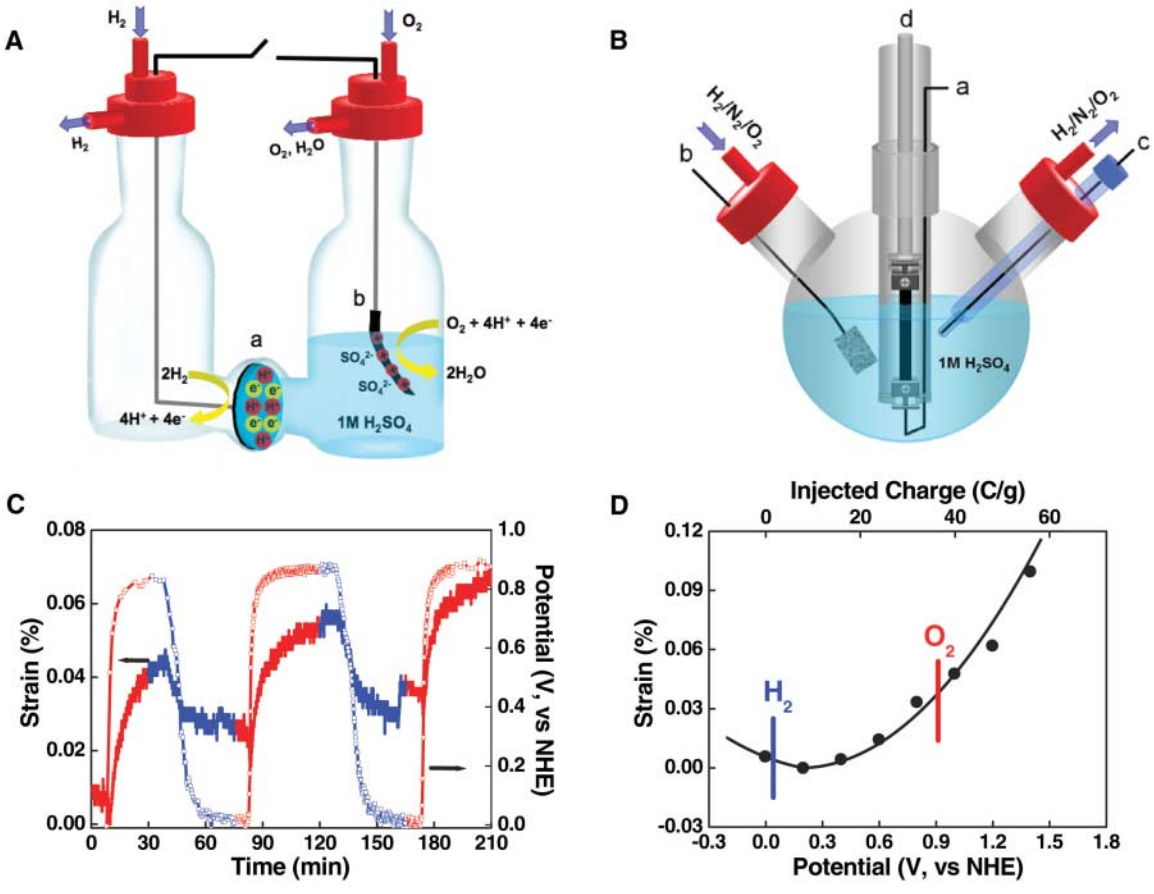

Fig. 1. Nanotube-based fuel-cell muscles. (**A**) Schematic illustration of the apparatus used for demonstration of a cantilever-based nanotube fuel-cell muscle. Element a is the membrane electrode assembly (composed of a porous carbon bilayer, a Pt-C-ionomer layer, and a Nafion-117 membrane) that is the counter-electrode to the actuating Pt-containing nanotube cantilever strip (element b). (**B**) Schematic illustration of a one-compartment cell mounted in a dynamic mechanical analyzer (DMA) for tensile measurements during either fuel-driven or electrically driven actuation. Elements a, b, and c are electrical wires connecting to the fuel-cell muscle working electrode (catalyst-containing nanotube sheet), the carbon felt counter-electrode, and the Ag/AgCl reference electrode, respectively. Element d is the measurement probe assembly of the DMA. (**C**) Potential and actuator strain versus time for a tensile nanotube actuator that is alternately exposed to pure O_2 (red) or a mixture of 5 volume % H_2 in inert gas (blue). An N_2 purge between the O_2 and H_2 purges has negligible duration on this time scale. The slow actuator response results from the present need to dissolve different gases in relatively massive amounts of electrolyte in different parts of the actuation cycle. Creep, which is also a problem for electrically powered nanotube sheet actuators, causes the irreversible component of actuator strain. (**D**) Measured tensile actuator strain versus potential and injected charge for an electrically powered nanotube actuator, indicating the measured hydrogen and oxygen potentials for the chemical actuator experiment. There is agreement between the strain change ongoing between these potentials in the fuel-powered and electrically powered actuator experiments.

second type of artificial muscle functions as a "continuously shorted fuel cell" that converts chemical energy in a fuel to thermal energy that produces actuation.

The first demonstration was of a cantilever actuator (Fig. 1A) in which a nanotube sheet strip was laminated with a mixture of Pt-coated carbon and Nafion ionomer (*21*). The actuating cantilever electrode was immersed in 1 M H_2SO_4, and the counter-electrode was a Pt-C-Nafion ionomer layer deposited on a Nafion-117 membrane, which separated the fuel (hydrogen, at the counter-electrode) from the oxidant (oxygen, at the nanotube actuator electrode) and enabled hydrogen ion diffusion between electrodes when the electrodes were shorted. Unlike traditional fuel cells, where the anode and cathode are deposited on each side of a proton-conducting membrane (such as Nafion), the anode and the cantilever-type cathode in our design are mechanically uncoupled but ionically connected to each other by a liquid electrolyte, enabling actuation during charge/discharge operation of the cell.

This fuel-cell muscle type is in part electrochemical and uses the catalyst-containing carbon nanotube sheet electrode as an artificial muscle. Although both the working and counter-electrodes can actuate, only one electrode was used for actuation in this initial demonstration. Reversible actuator strokes result from electronic charge injection into carbon nanotubes (*22*, *23*). The simultaneous movement of ions of the electrolyte into close proximity to the injected electronic charge forms the so-called electrochemical double layer, which enables high charge injection by maintaining overall charge neutrality. This close proximity of electronic charge on the carbon nanotubes and counter-ions in the electrolyte is enabled by the nanoscale porosity of the carbon single-walled nanotube (SWNT) sheets and the corresponding high surface area, ~300 $m^2\ g^{-1}$ (*23*).

Instead of actuating in response to an applied inter-electrode voltage, the chemically powered actuator electrode generates a potential by acting as a fuel-cell electrode. The fuel-cell muscle generates and capacitively stores electrical energy (which simultaneously causes actuation) when the inter-electrode circuit is open. Oxygen gas at the cantilevered nanotube electrode is reduced in the presence of Pt. Four protons in the H_2SO_4 combine with an O_2 and four electrons extracted from the carbon nanotube electrode to produce two water molecules. The resulting injection of positive charge (holes) into the nanotube sheet causes actuation, with the SO_4^{2-} ions serving as countercharges. Reaction continues until the nanotube electrode is fully charged, generating a half-cell potential of ~0.9 V versus that of a normal hydrogen electrode (NHE) (Fig. 1A). This differs from the continuous power production process of an ordinary hydrogen fuel cell, where the protons and electrons needed to produce water come from the hydrogen electrode. Also, unlike the case of electrically powered actuation using double-layer charge injection, the amount of charge injected into the two electrodes depends only on their individual charge storage capability.

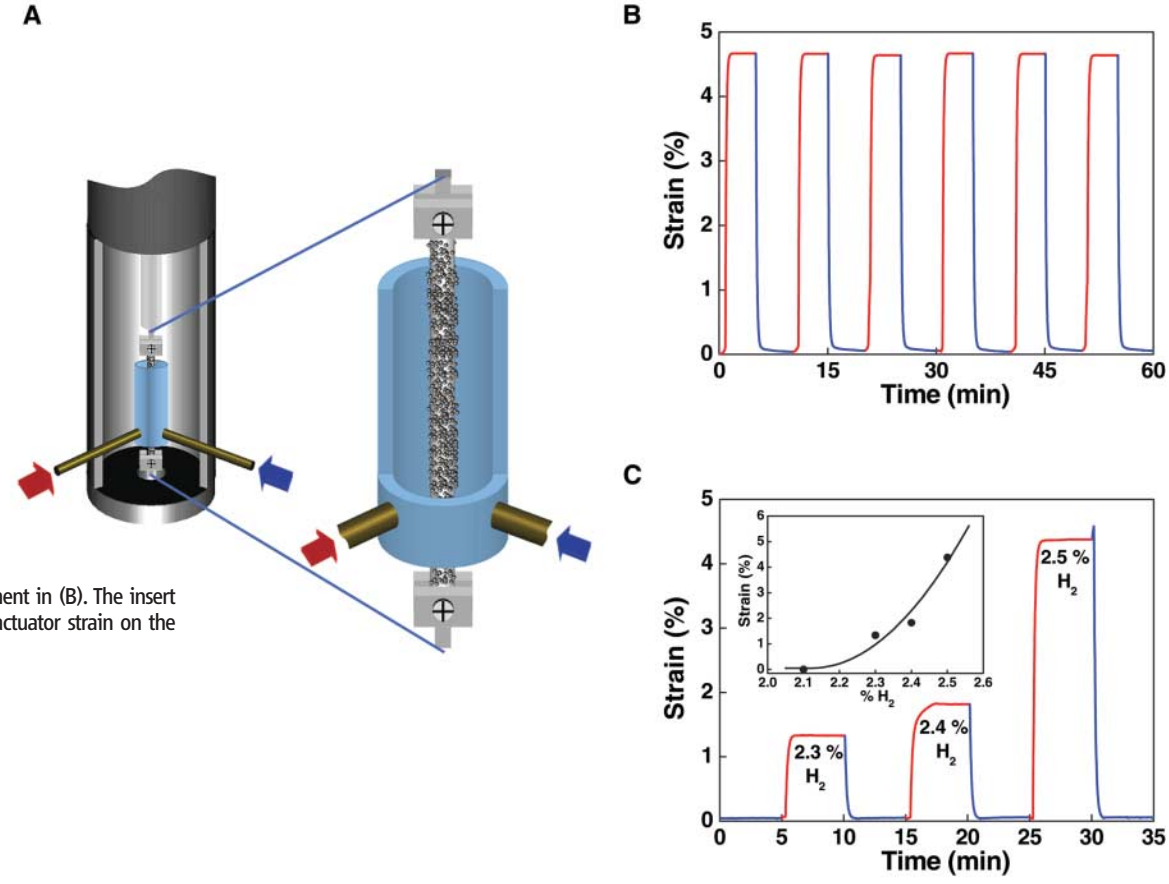

Fig. 2. Continuously shorted fuel-cell muscle based on a NiTi shape-memory alloy. (**A**) Schematic illustration, with cutaway to reveal details, of the fuel-powered artificial muscle mounted in the dynamic mechanical analyzer used for measurements. (**B**) Actuator strain versus time during exposure of the chemically powered actuator to a mixture of N_2, 2.5% by volume hydrogen and 50% oxygen (red curves) and during exposure to pure oxygen (blue curves). (**C**) Actuator strain versus time for different volume percents of H_2 for the experiment in (B). The insert shows the dependence of actuator strain on the H_2 volume % in the fuel.

At the opposite electrode, again under open circuit conditions, hydrogen is oxidized to produce protons and electrons that form an electrochemical double layer, generating a half-cell potential of 0.0 V versus NHE (Fig. 1A). The discharge of the fuel-cell muscle, where actuation is reversed, corresponds to the recombination of electrons on the hydrogen electrode with the holes on the oxygen electrode (the actuating nanotube sheet) when the inter-electrode circuit is closed. Simultaneously, the H_2-derived protons diffuse to the carbon nanotube cathode to replace H^+ ions in the liquid electrolyte that were used to make water during the hole-injection part of the actuator cycle.

The observed actuator stroke during chemically driven charge injection was a 2-mm deflection of a 3-cm-long nanotube cantilever in ~5 s, as the nanotube electrode potential increased to ~0.8 V (versus NHE) (fig. S1). The opposite actuator deflection, obtained when the hydrogen and oxygen electrodes were shorted, occurred in ~1 s (fig. S1). Breaking the connection between electrodes caused recharging of the nanotube muscle and return to the deflection of the initially charged state.

Although this fuel-cell muscle uses only one electrode for actuation, both electrodes can simultaneously serve as muscles. To demonstrate this, we switched the oxygen and hydrogen delivery, so that the actuator electrode became the hydrogen electrode. This causes a decrease in the time required for the charge-injection stroke to 1 to 2 s and a 180° phase shift in actuator response direction. This phase shift and unchanged actuation amplitude result from the low charge-storage capacity of the nanotube sheet as compared to that of the much larger counter-electrode. As a result, the nanotube electrode potential cycles between ~0 and ~0.9 V (versus NHE) during charge and discharge, and only the direction of this shift depends on the gas at the actuating electrode.

Again using hydrogen as the fuel, oxygen as the oxidant, and 1 M H_2SO_4 as the electrolyte, we also drove forward and reverse actuation of a Pt-containing nanotube sheet in a one-compartment cell (Fig. 1B). The fuel and oxidant were introduced one at a time, with an N_2 purge in between. Instead of using a cantilever actuator as the electrode, we used a nanotube sheet that was uniformly filled with catalyst and characterized actuation in tension (*21*). The actuation observed in this setup is driven by the same half-cell reactions as described in the previous two-compartment cell (Fig. 1A), where the fuel and oxidant are continuously present in separate compartments. Because the driving potential and electrolyte are unchanged, the basic mechanisms (quantum-mechanical and coulombic) (*23*) for causing changes in nanotube dimension should be identical.

In the forward actuation step, the nanotube sheet was double-layer charged to 0 V (versus NHE) by filling the cell with hydrogen. After purging the cell with N_2 to avoid direct contact of a H_2 and O_2 mixture with the catalyst, we filled the cell with O_2, which reversed the charging and actuation direction as the nanotube electrode went to a potential of ~0.9 V (versus NHE). Although very long actuation times result in this configuration from the need to periodically dissolve gases in relatively massive amounts of electrolyte, this experiment enabled a reliable comparison between chemically driven and electrically driven actuation in one electrolyte for the same type of Pt-infiltrated nanotube sheet. The obtained results (Fig. 1C) show that the potential changed from ~0.0 to ~0.9 V (versus NHE) as the hydrogen gas in the cell was switched to oxygen, and that the length increase of the nanotube sheet was ~0.035%. Essentially the same length change resulted for electrically driven actuation between these potentials in the utilized electrolyte (Fig. 1D). This actuation strain is within a factor of 3 of the typically 0.1% maximum strain for commercial high-modulus ferroelectrics, which usually require about 100 V of externally applied potential for operation (*1*).

Although the efficiencies of polymer electrolyte fuel cells do not exceed 40% at peak power (*24*), the second type of fuel-powered

muscle can use essentially all of the energy produced by fuel oxidation to produce the heating needed for actuation (*15*). This muscle is called a continuously shorted fuel-cell muscle because the effective redox reactions occur on a catalyst-coated shape-memory metal. Unlike the situation in a classical fuel cell, both fuel and oxidant are simultaneously delivered to a single electrode (a Pt-coated shape-memory wire), which functions as a shorted electrode pair.

Our demonstrations used a NiTi shape-memory wire coated with Pt catalyst particles as the fuel-cell muscle and either hydrogen, methanol, or formic acid as fuel (*21*). The Pt-coated shape-memory wire was attached to a sample holder of a dynamic mechanical analyzer and placed in an enclosure with provision for the simultaneous introduction of fuel and oxidant (Fig. 2A). Contact of the fuel and an oxidant (oxygen or air) causes the mechanically loaded wire to heat to above the austenitic phase-transition temperature and do mechanical work during the resulting contraction. Upon interruption of the fuel, the wire cools to below its martensitic phase-transition temperature and returns to its original length (Fig. 2, B and C).

This fuel-powered muscle (Fig. 2B) supported stress of ~150 MPa or more while undergoing ~5% contraction when powered by a mixture of oxygen (or air) and either methanol vapor, formic acid vapor, or a noncombustible mixture of hydrogen in inert gas. This stress-generation capability is ~500 times that which is typical for human skeletal muscle (0.3 MPa), whereas the percent stroke is ~25% that of this natural muscle (*1*). Hence, the work capability of the continuously shorted fuel-cell muscle on lifting a weight (5300 kJ m^{-3} for methanol and 6800 kJ m^{-3} for hydrogen or formic acid) is over 100 times that of skeletal muscle (~40 kJ m^{-3}) (*1*). The percent contraction (5, 7, and 8% observed for 150-, 122-, and 98-MPa loads, respectively, using 2.5 volume % hydrogen in inert gas as fuel) can be increased to far above the ~20% typical of skeletal muscle (*1*) by simply coiling the shape-memory wire, albeit with a proportional decrease in stress generation. The presently achieved power density (68 W kg^{-1} during the work part of the cycle for hydrogen fuel) is similar to that of natural skeletal muscle (typically about 50 W kg^{-1}) (*1*). By increasing the fuel delivery rate and optimizing fuel composition and catalyst loading, it should be possible to dramatically increase power density.

References and Notes

1. J. D. W. Madden *et al.*, *IEEE J. Oceanic Eng.* **29**, 706 (2004).
2. R. H. Baughman, *Science* **308**, 63 (2005).
3. E. Smela, *Adv. Mater.* **15**, 481 (2003).
4. R. Pelrine, R. Kornbluh, Q. Pei, J. Joseph, *Science* **287**, 836 (2000).
5. Q. M. Zhang, V. Bharti, X. Zhao, *Science* **280**, 2101 (1998).
6. S. Nemat-Nasser, *J. Appl. Phys.* **92**, 2899 (2003).
7. J. Weissmüller *et al.*, *Science* **300**, 312 (2003).
8. S. Hara, T. Zama, W. Takashima, K. Kaneto, *J. Mater. Chem.* **14**, 1516 (2004).
9. K. Asaka, K. Oguro, Y. Nishimura, M. Mizuhata, H. Takenaka, *Polym. J.* **27**, 436 (1995).
10. H. B. Schreyer, N. Gebhart, K. J. Kim, M. Shahinpoor, *Biomacromolecules* **1**, 642 (2000).
11. D. Kaneto, J. P. Gong, Y. Osada, *J. Mater. Chem.* **12**, 2169 (2002).
12. Y. Osada, H. Okuzaki, H. Hori, *Nature* **355**, 242 (1992).
13. O. K. Rediniotis, D. C. Lagoudas, H. Y. Jun, R. D. Allen, *Proc. SPIE* **4698**, 441 (2002).
14. R. H. Baughman, C. Cui, J. Su, Z. Iqbal, A. A. Zakhidov, U.S. patent 6,555,945 (2003).
15. R. J. Howard, U.S. Patent Application Publication U.S. 2005/0028901 (2005).
16. W. F. Paxton *et al.*, *J. Am. Chem. Soc.* **126**, 13424 (2004).
17. S. Fournier-Bidoz, A. C. Arsenault, I. Manners, G. A. Ozin, *Chem. Commun.* 441 (2005).
18. T. R. Kline, W. F. Paxton, T. E. Mallouk, A. Sen, *Angew. Chem. Int. Ed. Engl.* **44**, 744 (2005).
19. J. M. Catchmark, S. Subramanian, A. Sen, *Small* **1**, 202 (2005).
20. R. F. Ismagilov, A. Schwartz, N. Bowden, G. M. Whitesides, *Angew. Chem. Int. Ed. Engl.* **41**, 652 (2002).
21. Materials and methods are available as supporting material on ***Science*** Online.
22. R. H. Baughman *et al.*, *Science* **284**, 1340 (1999).
23. R. H. Baughman, A. A. Zakhidov, W. de Heer, *Science* **297**, 787 (2002).
24. F. Barbir, T. Gómez, *Int. J. Hydrogen Energy* **22**, 1027 (1997).

25. The authors thank J. A. Main for describing needs that led to this work and B. L. Lee for discussions of actuator energy harvesting. This work was supported by the Defense Advanced Research Projects Agency/U.S. Army Research Office (grant W911NF-04-1-0174), the Robert A. Welch Foundation (grant AT-0029), and the Strategic Partnership for Research in Nanotechnology (SPRING) consortium in Texas.

Supporting Online Material

www.sciencemag.org/cgi/content/full/311/5767/1580/DC1
Materials and Methods
Fig. S1

14 September 2005; accepted 19 January 2006
10.1126/science.1120182

Microstructured Optical Fibers as High-Pressure Microfluidic Reactors

Pier J. A. Sazio,[1*] Adrian Amezcua-Correa,[1] Chris E. Finlayson,[1†] John R. Hayes,[1] Thomas J. Scheidemantel,[2,3] Neil F. Baril,[2,4] Bryan R. Jackson,[2,4] Dong-Jin Won,[2,5] Feng Zhang,[2,3] Elena R. Margine,[2,3] Venkatraman Gopalan,[2,5] Vincent H. Crespi,[2,3,5] John V. Badding[2,4*]

Deposition of semiconductors and metals from chemical precursors onto planar substrates is a well-developed science and technology for microelectronics. Optical fibers are an established platform for both communications technology and fundamental research in photonics. Here, we describe a hybrid technology that integrates key aspects of both engineering disciplines, demonstrating the fabrication of tubes, solid nanowires, coaxial heterojunctions, and longitudinally patterned structures composed of metals, single-crystal semiconductors, and polycrystalline elemental or compound semiconductors within microstructured silica optical fibers. Because the optical fibers are constructed and the functional materials are chemically deposited in distinct and independent steps, the full design flexibilities of both platforms can now be exploited simultaneously for fiber-integrated optoelectronic materials and devices.

Optical fibers provide ideal hosts for the manipulation of photons, especially when formed into microstructured optical fibers (MOFs) that enable precise control of photon dispersion (*1*). Crystalline semiconductors such as silicon provide ideal hosts for the manipulation of electrons, especially when formed into heterostructures that enable precise control of electron transport. It has thus far not been possible to integrate the crystalline semiconductors that form the basis for modern optoelectronics into MOFs, allowing for interaction of such materials with waveguided electromagnetic radiation over much longer length scales than can be realized in typical planar device geometries (*2*). Fabrication of such structures would be a major step forward toward all-fiber optoelectronics. The preferred method for depositing semiconductors and metals, including nearly all of the technologically important semiconductors, is chemical vapor deposition (CVD) (*3*). However, CVD onto the walls of the long, extremely narrow pores in a MOF presents two challenges: Small deviation from perfect conformal deposition anywhere along the length of the pore would immediately arrest deposition, and mass transport of the reactants into and by-products out of such a confined space is prohibitively slow using traditional techniques. We report the fabrication of high-quality polycrystalline and single-crystal semiconductors within the voids of MOFs by high-pressure microfluidic chemical deposition. High-pressure flow, which can be sustained because of the very